Journal of the European Ceramic Society 46 (2026) 118550

Contents lists available at ScienceDirect

Journal of the European Ceramic Society

journal homepage: www.elsevier.com/locate/jeurceramsoc

Carbon and sintering of oxides: Densification kinetics vary by orders of magnitude

Etienne Martin [a], Levent Karacasulu [b], Rajat Chaudhary [b], Wayne D. Kaplan [c], Rachel Marder [c], Thomas Herisson de Beauvoir [a], Claude Estournès [a], Mattia Biesuz [b,d,*]

[a] CIRIMAT, Université de Toulouse, Toulouse INP, CNRS, 118 Route de Narbonne, Toulouse 31062, France
[b] University of Trento, Department of Industrial Engineering, Via Sommarive 9, Trento 38123, Italy
[c] Department of Materials Science and Engineering, Technion – Israel Institute of Technology, Haifa 32000, Israel
[d] INSTM, Via Giuseppe Giusti, 9, Firenze 50121, Italy

ARTICLE INFO

Keywords:
Sintering
Carbon
Dilatometry
Spark plasma sintering
Grain growth

ABSTRACT

Advanced ceramics manufacturing (e.g., non-conventional sintering, additive manufacturing…) often introduces carbonaceous species into oxides. Herein, we investigate the carbon impact on the densification kinetics in model systems (Al_2O_3 and Y_2O_3-stabilized ZrO_2). While the influence of carbon may be limited in the case of pressure-assisted densification, its impact in pressure-less processes is significant: the addition of ≈ 0.5 wt% of carbon delays consolidation by hundreds of degrees Celsius. Such an effect is also visible when the carbon doping occurs after pre-sintering, i.e., after the formation of the first necks and grain boundaries. Besides densification, grain growth is substantially affected. The observed change in the densification kinetics is consistent with a decreasein the driving force induced by the carbon adsorption on the powder surface, although additional effects might also occur. These results are of particular relevance given that different sources of carbon are emerging in ceramic processing from additive manufacturing to non-conventional sintering.

1. Introduction

Over the past decade, the interaction between carbon and oxides has emerged as a focal point in materials research. This growing attention has been driven by both (i) the intentional incorporation of carbon nanomaterials to engineer ceramic properties and (ii) unintentional carbon contamination resulting from materials processing. The addition of carbon-nanomaterials, such as graphene or carbon nanotubes, can improve the mechanical properties, including bending strength and fracture toughness [1–6], or introduce functional properties such as thermal and/or electrical conductivity [7–9]. Furthermore, carbon contamination can originate from material processing. Modern heating systems based on graphite (heating) elements, ranging from conventional graphite furnaces and hot-pressing machines to non-conventional sintering tools like spark plasma sintering (SPS) [10–12] and ultrafast high temperature sintering (UHS) [13–15], are increasingly studied and used.

The development of ceramic additive manufacturing (AM) has also introduced a new source of carbon contamination. In fact, the green systems produced by AM typically contain a large amount of organics (up to about 50 vol% in the case of vat photopolymerization of fused deposition modelling) [16]. The removal of the organics is crucial and typically requires several hours or even days. It has been recently shown that UHS, thanks to the use of an inert atmosphere, can substantially accelerate the debinding process, which in some cases can be reduced to a few minutes or even seconds [17–20]. However, this processing route leaves a small amount of carbon contamination within the ceramic [18].

It is known that carbon precipitates in the form of a secondary phase, primarily at triple junctions and grain boundaries, when its concentration exceeds the solubility limit [21]. Although precise carbon analysis by electron microscopy is not trivial, at carbon concentrations below the solubility limit, Gibbsian segregation of carbon at grain boundaries in alumina has been experimentally observed in 0.036 wt% C-doped alumina (1.5 ± 0.5 C atom nm^{-2}) [21]. This indeed has an impact on the grain growth kinetics through the particle drag (Zener drag) or solute drag effect [22] and could impact the final microstructure [23].

However, not much is known about the impact of carbon on the densification process of oxide ceramics. The only pertinent report is a

* Corresponding author at: University of Trento, Department of Industrial Engineering, Via Sommarive 9, Trento 38123, Italy.
E-mail address: mattia.biesuz@unitn.it (M. Biesuz).

https://doi.org/10.1016/j.jeurceramsoc.2026.118550
Received 7 January 2026; Received in revised form 19 May 2026; Accepted 24 May 2026
Available online 29 May 2026

publication by Cohen et al. [24] showing that if the carbon contamination exceeds the solubility limit in alumina (≈ 0.5 at% at the selected sintering temperature of 1600°C), then the ceramics are not fully densified. Such a result aligns with earlier literature by Mizardo et al. from the early '90 [25]. However, a detailed and quantitative description of the interaction between carbon contamination and consolidation is still missing and suffers from limited experimental work focusing only on a single oxide system, alumina.

Based on the interest in nanocomposites, the development of additive manufacturing and non-conventional sintering, it is important to understand whether and how carbon can interact with the densification process. This manuscript aims to identify the C effect on the sintering of two model ceramic systems, namely alumina and 3 mol.% Y-doped zirconia (YSZ).

2. Materials and methods

Different oxide powders have been used in this work. Alumina samples were obtained using ready-to-press (RTP) granulated powder CT3000SG provided by Almatis (99.8% pure, $d_{50} \approx 400$ nm). The 3YSZ was purchased from Tosoh, and the following grades were used: TZ−3Y-E (40 nm particle size, not granulated), TZ−3YB-E (40 nm particle size, RTP-granulated), and TZ−3YSB-E (90 nm particle size, RTP-granulated). The saccharose used as a carbon source was purchased from Sigma Aldrich (BioUltra, for molecular biology, ≥ 99.5% 84097 Sigma Aldrich). Indeed, during thermal treatments in an inert atmosphere, saccharose decomposes via pyrolysis, leaving a small amount of residual carbon. The carbon yield estimated by TGA/DSC (10°C min^{-1} in Ar, Netzsch STA Jupiter) is about ≈ 16.2% (Fig. 1). The decomposition mostly occurs between 220 and 400°C, with residual weight loss up to about 600°C. The DSC shows the saccharose melting (≈170°C) and some endothermic effects related to the decomposition.

Note that we decided to use saccharose as a carbon source (rather than some solid C phase) due to its solubility in water, guaranteeing a homogeneous deposition of C (after pyrolysis on the powder). It also allows C-doping on pre-sintered samples by infiltrating the material with a saccharose syrup, as will be detailed later.

Two different strategies were adopted to add saccharose to the oxide (Fig. 1). In a first experiment, 75 wt% of TZ−3Y-E was mixed with 25 wt % of saccharose in a mortar, and water was added until a homogeneous paste was obtained and all the saccharose dissolved. The paste was then dried and used to obtain pellets by uniaxial pressing under 350 MPa using a steel die. The sample size was 8 mm in diameter with a thickness of about 3 mm. When sintering was carried out in an inert atmosphere (Ar), saccharose decomposes, resulting in about 5 wt% of carbon (measured by weighing the sample before and after the saccharose decomposition). Such a figure matches very closely the theoretical C yield computed from the TGA data (16.2 wt%) and the initial saccharose load in the green (25 wt%), hence, the TGA carbon yield provides a good approximation of the pyrolysis in the dilatometer.

A second strategy was applied for TZ−3YSB-E RTP-YSZ and for alumina (Almatis CT300SG). In this case, the green bodies were first shaped by uniaxial pressing under the same conditions mentioned above. The bodies were then pre-sintered at 1100°C with no holding time and using a heating rate of 10°C min^{-1} in a Nabertherm muffle furnace in air. The shrinkage was negligible during the treatment, and the pre-sintered densities were about 49% and 58% of the theoretical ones for YSZ and alumina, respectively. Then, the ceramics were immersed in a saccharose syrup (20 wt% of saccharose in water) and vacuum infiltrated. After infiltration with the syrup, the samples were dried in an oven at 100°C overnight, and the saccharose content was estimated based on the weight gain (≈ 3.8 wt% in alumina and 3 wt% in YSZ). After sintering in an inert atmosphere, the resulting carbon yield was about 0.6 wt% and 0.5 wt% for alumina and YSZ, respectively. These figures were computed from the initial saccharose load and the carbon yield of pure saccharose from TGA (16.2 wt% from Fig. 1). The validity of this approach was corroborated by the carbon load estimation from the weight measurements on the samples containing 25 wt% of saccharose as previously discussed. Note that this calculation represents the upper limit for the C content that can decrease, especially at high temperatures, due to the reactions with oxygen impurities in the atmosphere or by partially reducing the oxide. The latter effect is

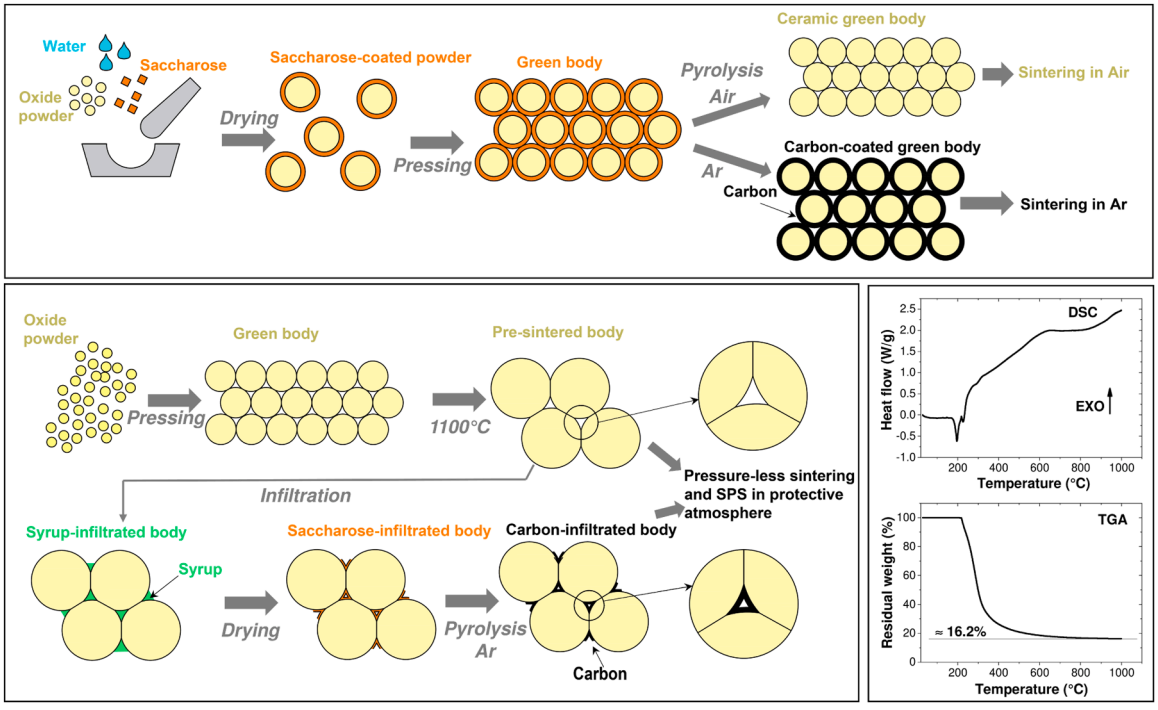

Fig. 1. Schematic of the different sample preparation procedures: (top panel) saccharose added before shaping the green body; (bottom left) saccharose addition after pre-sintering. (bottom right) TGA/DSC analysis of the saccharose in Ar.

particularly relevant for YSZ, as will be shown later. Some pre-sintered samples were not infiltrated to have a saccharose (carbon)-free reference material; these serve as a benchmark for all the measurements.

The sample labelling throughout the manuscript is as follows:

- The first letters refers to the type of powder (A = alumina; $YSZ_{90\ nm}$ = 90 nm-sized 3 mol% YSZ; $YSZ_{40\ nm}$ = 40 nm-sized 3 mol% YSZ);
- The amount of saccharose (if any) is reported as a number (wt%) followed by "s";
- Except for $YSZ_{40\ nm}$-25s-g, all green bodies were pre-sintered at 1100°C before the sintering experiments. Some of these samples were vacuum infiltrated with saccharose syrup, while others were not so as to provide control samples. As this experimental methodology (pre-sintering at 1100°C) applies to almost all samples, it is implicitly suggested and not mentioned in the labelling. In the case of the sample $YSZ_{40\ nm}$-25s-g, the last letter "g" refers to the procedure used to add the saccharose, i.e., the addition of saccharose to the powder before shaping the green bodies.

A summary of all the samples and the different sintering tests that were carried out is reported in Table 1, along with the reference labelling.

The said samples were then used for various sintering experiments. Dilatometric tests were carried out in inert (Ar) or oxidizing (air) atmosphere using a contact dilatometer Linseis L75 equipped with an alumina measurement system. In some cases, the sintering atmosphere was switched from Ar to air during the test (the details about the sintering atmospheres are clearly underscored in the different figures). The gas flux was about 200 $cm^3.min^{-1}$. To reduce oxidation of the carbon produced by the saccharose decomposition, a small piece of graphite felt was introduced into the dilatometer chamber. Based on the green density and the measured dilatometric shrinkage, the density evolution was estimated under an isotropic shrinkage assumption.

Some green pellets were then pressure-less sintered in a RKC 800 Lindberg alumina tubular furnace. The temperature was increased at a rate of 10 °C min^{-1} up to the maximum temperature, followed by a 30 min isothermal hold. The samples were then allowed to cool naturally to room temperature. Three sintering temperatures (1200 °C, 1300 °C, and 1500 °C) and two atmospheres (air and Ar) were used, yielding six distinct sample sets. Before sintering, temperature calibration was performed at the sample positions with an S-thermocouple. For samples sintered in Ar, a carbon felt (SGL Carbon Co.) was placed near the specimens to reduce the oxidation of carbon in the samples by oxygen impurities in the chamber.

The consolidation of Al_2O_3 and YSZ ceramics by SPS was performed with a 632LX model (Fuji Electronic Industrial CO., Japan) at the Plateforme Nationale CNRS de Frittage Flash (University of Toulouse), using graphite dies (Ø 8 mm in diameter), spacers, and punches. Before the thermal cycle begins, a vacuum of 20 Pa was achieved in the SPS chamber using a primary pump. Argon was then introduced into the chamber until atmospheric pressure was restored. For these experiments, a direct current pulse pattern of 40 ms on: 7 ms off was used, and the temperature was measured by an optical pyrometer focused on the outer surface of the die. A preheating step at 300°C min^{-1} until 600°C was carried out to reach the pyrometer's detection threshold and decompose the saccharose. During this step, the uniaxial pressure was also gradually applied over 3 min. After 2 min of dwell at 600 °C to homogenize the temperature throughout the sample, a heating ramp of 50 °C/min was set until the final target temperature, either 1150 °C, 1250 °C, 1350, or 1500 °C, depending on the experiment. The relative density of these SPS ceramics was evaluated by Archimedes' method with impregnation of the pellets in ethanol. The relative density was determined by accounting for the residual carbon in the system.

In order to plot the densification curves for the SPS experiments throughout the thermal cycle, the instantaneous density of the samples was evaluated based on the measured instantaneous vertical shrinkage, the final density, and the final thickness. Although the distance between the two electrodes of the SPS device can be measured throughout the densification process, it is nevertheless essential to deduce, from the raw measurements, the contribution corresponding to the expansion of the graphite column during the thermal cycle. Thus, blank experiments (without samples) were carried out under all the experimental conditions studied. The thermal expansion of YSZ and alumina powders was also considered, with a thermal expansion coefficient α (YSZ) = 10 K^{-1} and α (Al_2O_3) = 8.5 K^{-1}, respectively.

The instantaneous relative density was thus determined from the vertical shrinkage of the sample during densification by SPS. Knowing the final thickness of the sample e_f and its final relative density D_f (measured by three-weighing Archimedes' method), measurements of the instantaneous thickness of the sample e_i can be used to determine D_i, $D_i = \frac{D_f}{e_i} e_f$.

In order to obtain chemical and structural characterizations of the samples sintered at different temperatures, Raman spectroscopy was

Table 1
List of samples and processing methods used in this study.

Label	Sintering method	Ceramic (wt% in the green body)	Saccharose (wt% in the green body)	C (wt% after pyrolysis)	Pre-treatments
$YSZ_{40\ nm}$-25s-g	Dilatometer (20°C min^{-1})	75 wt% 3 mol%YSZ (40 nm Tosoh)	25	≈ 5 in Ar 0 in air	Saccharose addition to the powder before shaping
A-4s	Dilatometer (10°C min^{-1}) Conventional sintering in a tube furnace (10°C min^{-1}, 30 min dwell) SPS (Ar, 50°C min^{-1}, 5–80 MPa)	96.2 wt% Al_2O_3 (CT300SG, RTP Almatis)	3.8	≈ 0.6	Infiltration with saccharose syrup after pre-sintering at 1100°C (no holding, heating rate 10°C min^{-1})
A	Dilatometer (10°C min^{-1}) Conventional sintering in a tube furnace (10°C min^{-1}, 30 min dwell) SPS (Ar, 50°C min^{-1}, 5–80 MPa)	100 wt% Al_2O_3 (CT300SG, RTP Almatis)	0	0	Pre-sintering 1100°C (no holding, heating rate 10°C min^{-1})
$YSZ_{90\ nm}$-3s	Dilatometer (10°C min^{-1}) Conventional sintering in a tube furnace (10°C min^{-1}, 30 min dwell) SPS (Ar, 50°C min^{-1}, 5–80 MPa)	97.0 wt% 3 mol%YSZ (90 nm, RTP Tosoh)	3.0	≈ 0.5	Infiltration with syrup after pre-sintering at 1100°C (no holding, heating rate 10°C min^{-1})
$YSZ_{90\ nm}$	Dilatometer (10°C min^{-1}) Conventional sintering in a tube furnace (10°C min^{-1}, 30 min dwell) SPS (Ar, 50°C min^{-1}, 5–80 MPa)	100 wt% 3YSZ (90 nm, RTP Tosoh)	0	0	Pre-sintering 1100°C (no holding, heating rate 10°C min^{-1})
$YSZ_{40\ nm}$-3s	SPS (Ar, 50°C min^{-1}, 5–80 MPa)	97.0 wt% 3 mol%YSZ (40 nm, RTP Tosoh)	3.0	≈ 0.5	Infiltration with syrup after pre-sintering at 1100°C (no holding, heating rate 10°C min^{-1})
$YSZ_{40\ nm}$	SPS (Ar, 50°C min^{-1}, 5–80 MPa)	100 wt% 3 mol%YSZ (40 nm, RTP Tosoh)	0	0	Pre-sintering 1100°C (no holding, heating rate 10°C min^{-1})

performed using a confocal micro-Raman microscope LabRAM HR 800 (HORIBA Scientific, Jobin-Yvon). The spectra were acquired from fracture surfaces, pointing locally at the center of pellets. The analyses were performed with a green laser ($\lambda = 532$ nm), and the Raman spectra were collected in a backscattering configuration using a confocal microscope equipped with a long working distance x100 objective (focal distance of 3 mm). The spectra were recorded with a 600 lines/mm grating, inducing a spectral resolution of 2 cm^{-1}. The focused laser beam had a spot size of ≈ 700 nm and an axial resolution of 2.6 μm. Each spectrum is an average of 4 accumulations recorded with an exposure time of 16 s in the range from 100 to 1800 cm^{-1}.

X-ray Photoelectron Spectroscopy (XPS) analyses were carried out on a ThermoFisher Scientific K-ALPHA spectrometer with a monochromatized Al Kα source ($h\nu = 1486.6$ eV) and a 400 μm X-ray spot size. Prior to characterization, the pellets were fractured. Angle-resolved measurements were performed at a take-off angle $\theta = 90°$ (e.g., normal to the sample fracture surface). The sample holder was directly placed into vacuum and transferred into the analysis chamber when the pressure reached 5.10^{-7} Pa.

Scanning electron microscopy (SEM, Zeiss Ultra Plus FEG SEM) operated at 1.5–4.15 kV was used for microstructural inspection of fracture surfaces of the conventionally sintered specimens. No carbon coating was applied before inspection in order not to add additional carbon to the samples.

SEM analysis of the fracture surfaces of the SPS samples was performed using a SEM TESCAN VEGA 3 (tungsten filament) at CIRIMAT (University of Toulouse). In order to optimize charge evacuation during analysis, samples were metallized by PVD deposition of a Au/Pd layer. SEM images were obtained using a secondary electron detector, at a working distance of 10 mm and with an acceleration voltage of 20 kV. The mean grain size of SPS ceramics was evaluated based on an average of 250 individual grain measurements taken from four micrographs of different areas for each sample, to obtain a reliable value characteristic of the ceramics as a whole. No correction factor was applied to the mean grain size values.

3. Results

The sintering shrinkage of YSZ is substantially retarded when the bodies, including 25 wt% of saccharose, are fired in Ar rather than in air (pink and blue curves in Fig. 2a). The sintering curve in air appears regular with a shrinkage onset around 950°C; the plot starts flattening around 1300°C, and the final shrinkage at 1500°C exceeds 20%. On the other hand, the sample fired in Ar, which contains about 5 wt% of C due to the saccharose decomposition, is less prone to densification. No substantial shrinkage can be detected up to 1400°C, and even at 1500°C, the shrinkage is below 10%. Some additional densification can be noted in the cooling path. In some experiments, the sintering atmosphere was switched from Ar to air during the heating paths (green curves in Fig. 2a). We can notice that the body starts to shrink 2–3 min after the atmosphere was changed (≈ 50°C in the dilatometric plot obtained under 20 °C min^{-1}). Remarkably, these materials shrink more during cooling than during the heating path, even if the free cooling of the dilatometry furnace was much faster than the heating schedule.

Given this exceptional difference in the consolidation pathway induced by the oxidizing/inert environment, a second set of experiments on pre-sintered bodies was carried out. In this case, the pre-sintered oxides were infiltrated with a saccharose syrup (Fig. 2b) and sintered in an inert environment (Ar). Benchmark pre-sintered samples without carbon doping (i.e., without infiltration with saccharose syrup) were also sintered in the same atmosphere to exclude any atmosphere-related effect on densification. Furthermore, the total amount of carbon after pyrolysis of the infiltrated sample is substantially lower than in the previous case (≈ 0.5 wt%). Despite the low carbon load and even though the material was pre-sintered (hence it already contains some inter-particle necking before the infiltration with the syrup), a substantial difference in the dilatometric behavior was again observed; the sample containing C from the saccharose pyrolysis densifies at higher temperatures. However, the sintering delay is certainly reduced compared with the previous case. We can also observe the presence of a strange inflection around 1250°C in the sintering curve of the $YSZ_{90\ nm}$-3s sample, as well as some swelling in the final part of the test.

To generalize the results, we conducted a similar analysis on alumina (Fig. 2c). Also in this case, the samples were first pre-sintered and then infiltrated with saccharose. Similar to the YSZ, also in alumina the densification is delayed by a relatively small amount of C (about 0.6 wt %). The effect appears stronger than what was previously observed in YSZ, and the sintering curve with C appears more “regular”. It is remarkable to observe that 0.6 wt% of C prevents sintering up to temperatures exceeding 1400°C, and the final shrinkage at 1550°C is about 6% (less than half of the shrinkage measured from the sample without carbon). When considering the syrup-infiltrated sample, a change in the atmosphere while heating significantly impacts the consolidation (green curve in Fig. 2c). In fact, after air is introduced in the chamber, the sample starts to shrink quickly, approaching the sintering curve of the non-infiltrated material.

To validate the results, we conducted sintering experiments in a tube furnace (under Ar) on the pre-sintered alumina and YSZ, both with and without saccharose infiltration. We emphasize that, in this case, the samples were covered with graphite felt to minimize the oxidation of carbon in the samples by reacting with oxygen impurities in the atmosphere. The relative density development of these samples is shown in Fig. 3. The data indicate a significant impact of carbon infiltration on the final density, consistent with the dilatometric plot. This delayed consolidation is especially evident up to 1300°C in YSZ (density difference approaching 20%), while at 1500°C, the infiltration effect is less pronounced. Conversely, the alumina sample consistently exhibits a notable reduction in density caused by the presence of carbon.

The SEM micrographs (Fig. 4) of the fracture surfaces corroborate the said density evolution. The microstructure of YSZ at 1300°C shows significant differences between $YSZ_{90\ nm}$-3s and $YSZ_{90\ nm}$ samples, while both samples appear nearly fully dense at 1500°C with dominant intragranular fracture. On the other hand, the saccharose infiltration in alumina delays the densification even at 1500°C. In fact, A-4s fired at 1500°C still possess a very porous microstructure with minimal densification and reduced particle coarsening. On the other hand, its carbon-free counterpart (A) appears nearly fully dense at 1500°C, and substantial grain growth can also be noticed.

Some SPS tests were carried out on the pre-sintered samples with and without syrup-impregnation; the density evolution (Fig. 5) was estimated based on the displacement of the SPS tooling. While the data cannot be considered fully accurate, as in a regular dilatometric test, we can notice that the consolidation of the carbon-contaminated sample is again delayed. However, the delay appears substantially reduced, and in some cases fully nullified, when compared with the pressure-less sintering experiments in the dilatometer. In general, the carbon effect on the densification is weaker when the SPS pressure increases from 5 to 80 MPa.

Fig. 6 and Fig. 7 report some micrographs (fracture surfaces) of infiltrated and non-infiltrated samples after SPS (5 MPa) at different temperatures. The micrographs confirm that carbon induces some delay in the consolidation. Besides this, grain growth is substantially reduced by the presence of carbon, especially in alumina. The density measured on these samples, as well as the estimated grain growth, is reported in Fig. 8a,c. We can discern that the maximum density difference between samples with and without carbon in SPS under 5 MPa is ≈ 10%; a value substantially lower than what was observed in pressure-less sintering, ≈ 20% (Fig. 3). The grain size evolution shows a modest difference between the two batches of samples in the early-intermediate sintering stages, while the grain size in the final stage is substantially smaller when carbon is added. This effect is more visible in alumina, where the grain size is extremely stable even at 1500°C in the presence of carbon.

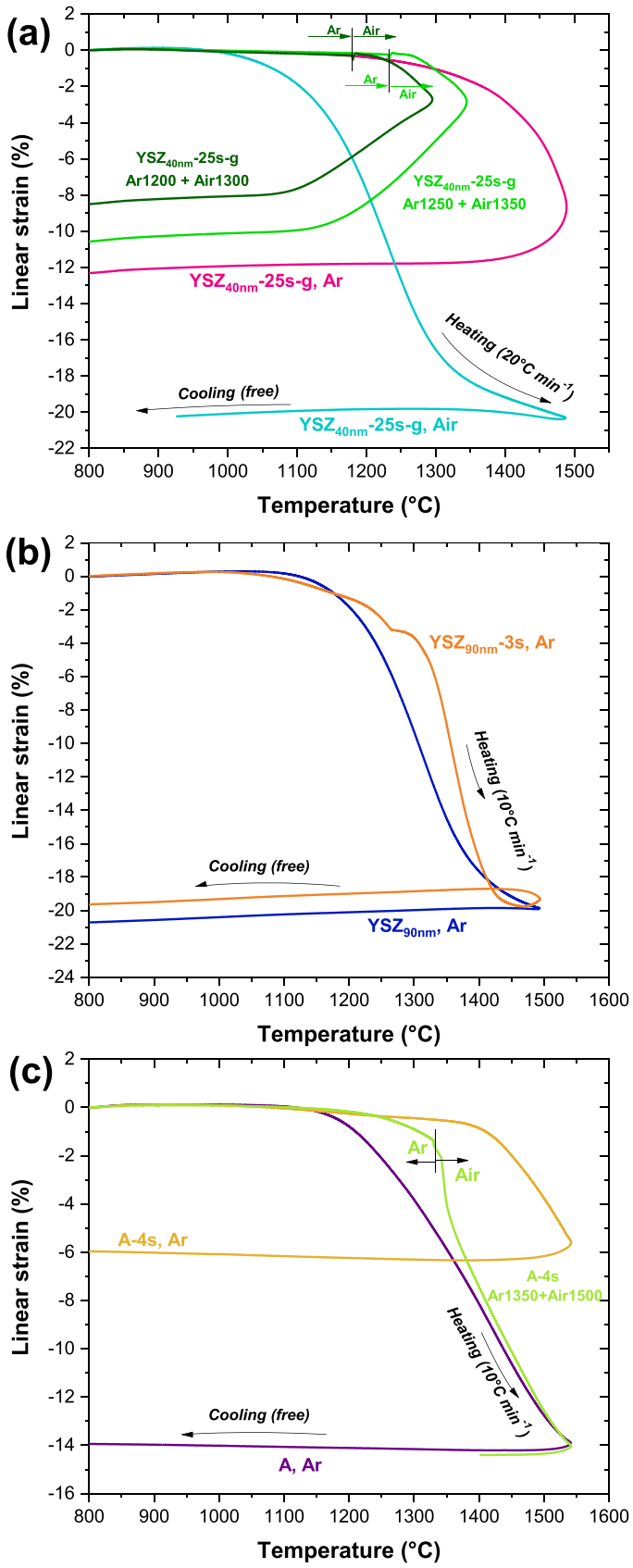

Fig. 2. Dilatometric analysis of YSZ and alumina under different heating rates with and without carbon contamination. (a) Comparison between YSZ containing 25 wt% of saccharose fired in air, Ar, and mixed atmosphere; comparison between the sintering behavior of pre-sintered (b) YSZ and (c) alumina with and without infiltration of saccharose (Ar and mixed atmosphere). The term "mixed atmosphere" means that the treatment was carried out in Ar up to a certain temperature, and then completed in air to oxidize the carbon deposits.

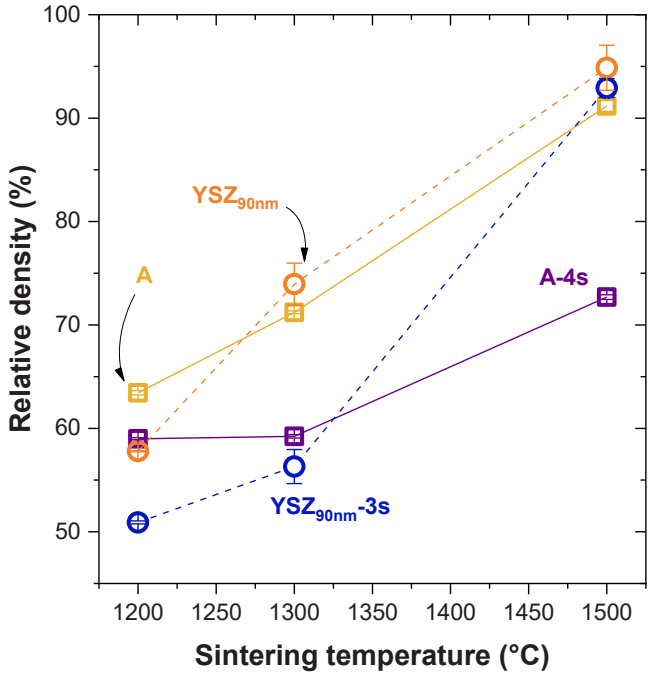

Fig. 3. Relative density of alumina and YSZ as a function of the final sintering temperature (Ar atmosphere). The samples were pre-sintered at 1100°C, and the carbon-containing samples were infiltrated with saccharose syrup before the sintering cycle (A-4s and $YSZ_{90\ nm}$-3s).

The grain size *vs.* density evolution is reported in Fig. 8b,d; it confirms that the grain size is substantially bound to density (irrespectively of the carbon doping) until the final sintering stages are reached (i.e., the data points of C-doped and C-free samples largely overlap).

The Raman spectra collected from the center of the samples after conventional sintering are reported in Fig. 9. The low-energy part of the spectrum is dominated by small features related to the oxide's structure. These are more visible in the case of YSZ samples and are fully related to the tetragonal or monoclinic polymorph of zirconia [26,27]. The two main Raman bands are located at 1335 – 1345 cm^{-1} and 1585 −1595 cm^{-1} and can be attributed to the D and G bands of carbon [28–31]. In alumina, the two bands are already quite defined and narrow at 1200°C, and the shoulder at about 1615 cm^{-1} is related to defect structures associated with a weaker D' band. Increasing the temperature up to 1300°C causes modest modification of the carbon phase, while at 1500°C the bands become narrower and the D' band can be identified as a clear small peak rather than a shoulder of the G band. There is also a substantial increase in the relative intensity of the G band over the D band. When considering YSZ, the D and G bands at 1200°C are extremely broad; they become narrower at 1300°C, resembling those in alumina at the same temperature. At 1500°C, the carbon-related bands fully disappear from the center of the sample.

To assess the possible reaction between YSZ and carbon at high temperature, XPS was performed on the samples SPSed at 1500°C with and without saccharose infiltration (Fig. 10). The choice of the sample is justified based on the fact that no oxygen contamination from the atmosphere is expected in the SPS chamber. The Zr3d spectrum is dominated by two main peaks located at about 181.3 and 183.7 eV, corresponding to $Zr3d_{5/2}$ and Zr $3d_{3/2}$. No additional features were noticed around 179 and 181.5 eV that could signal the formation of Zr-C bonds [32,33]. The shape of the carbon signal of the infiltrated samples is comparable with that of the non-infiltrated material. The latter possesses a lower signal-to-noise ratio resulting from a larger amount of carbon (note that carbon contamination is also possible in the carbon-free sample because of the graphite tooling of SPS [24]). The line-shapes are in both cases compatible with the spectrum originating from C-C bonds and possible organic contaminations (always present in the SPS chamber) C-H, C-O, C═O [34]. In both samples, no peaks can be detected around 182 eV, which would signal the formation of C-Zr bonds [32,33].

4. Discussion

4.1. Phenomenological effect

The dilatometric and density measurements (Figs. 2 and 3) indicate that carbon has a substantial influence on the sintering of YSZ and alumina, regardless of the initial particle size, heating rate, or sintering furnace. Specifically, the presence of carbon plays a crucial role in controlling the kinetics of densification, slowing down the consolidation. Note that this statement applies to systems where carbon remains present as a secondary phase or adsorbed on the surfaces/grain boundaries; different conclusions might arise if carbon reacts with the ceramic matrix. The latter is, for instance, the case of YSZ in the latter sintering stages.

We stress that the differences in the consolidation pathway are carbon-induced and are not related to any other possible contamination from the processing with saccharose (the purity was 99.5%). In fact, when the atmosphere is switched from Ar to air during heating for the carbon-containing sample, the consolidation accelerates because of carbon oxidation, moving the system closer to the undoped samples. Note, for instance, that when carbon is oxidized, the samples with and without saccharose infiltration behave similarly (Fig. 2c).

When a large amount of carbon precursor is added before shaping, its impact on densification is extremely relevant (Fig. 2a). However, only a modest amount of carbon (≈ 0.5 wt% introduced by syrup infiltration), which can easily occur due to debinding in an inert atmosphere, also has a significant impact. In fact, the samples infiltrated with the syrup have remarkably delayed densification when compared with the non-infiltrated material (Fig. 2b,c and Fig. 3). The difference is more "persistent" in alumina than in YSZ (i.e., in alumina, the difference can still be detected at 1500°C). This can be related to the relatively high reactivity of zirconia towards carbon: YSZ is more easily reduced, reacting with carbon, which leaves the sample before 1500°C. This statement is supported by the Raman spectra (Fig. 9), highlighting that the carbon phase in alumina is present after conventional sintering in Ar at 1500°C, while it fully disappears in YSZ at the same temperature (even from the center of the sample). Since the sintering atmosphere for the two powders was the same, we can infer that such a difference is related to the reactivity of carbon toward the oxides. In fact, it is not unusual that carbon contamination disappears at high temperature in YSZ by reacting with the oxide, slightly reducing it (formation of Zr^{3+}) [18]. The fact that the carbon phase is removed as a gas (CO/CO_2) is supported by the absence of any Zr-C bonds in the XPS spectra of C and Zr, thus excluding the formation of carbide (Fig. 10).

Carbon removal from the infiltrated-YSZ during sintering is likely related to the unusual dilatometric curve observed in Fig. 2b. The inflection around 1280°C might signal the beginning of the reduction of zirconia induced by carbon. Note that Zr^{3+} ($r = 0.89$ Å) is larger than Zr^{4+} ($r = 0.79$ Å) [35], thus likely causing a unit cell expansion that could explain why the shrinkage suddenly slows down. While this effect is not largely documented in YSZ (due to the relatively high stability of ZrO_2), it is widely known that other oxides with similar structures, like CeO_2 (prone to reduction), expand when reduced [36]. It is worth noting that after the said inflection point, the densification of the saccharose-infiltrated YSZ substantially accelerates, together with the removal of the carbon phase. When most of the porosity is closed (final sintering stage), the presence of some remaining carbon further produces gaseous C-oxides, causing the observed swelling above 1460°C (Fig. 2b). On the other hand, the lower reactivity of alumina toward carbon, testified by the substantial presence of D, G, and D' bands after sintering at 1500°C (Fig. 9), explains why its sintering behavior is more

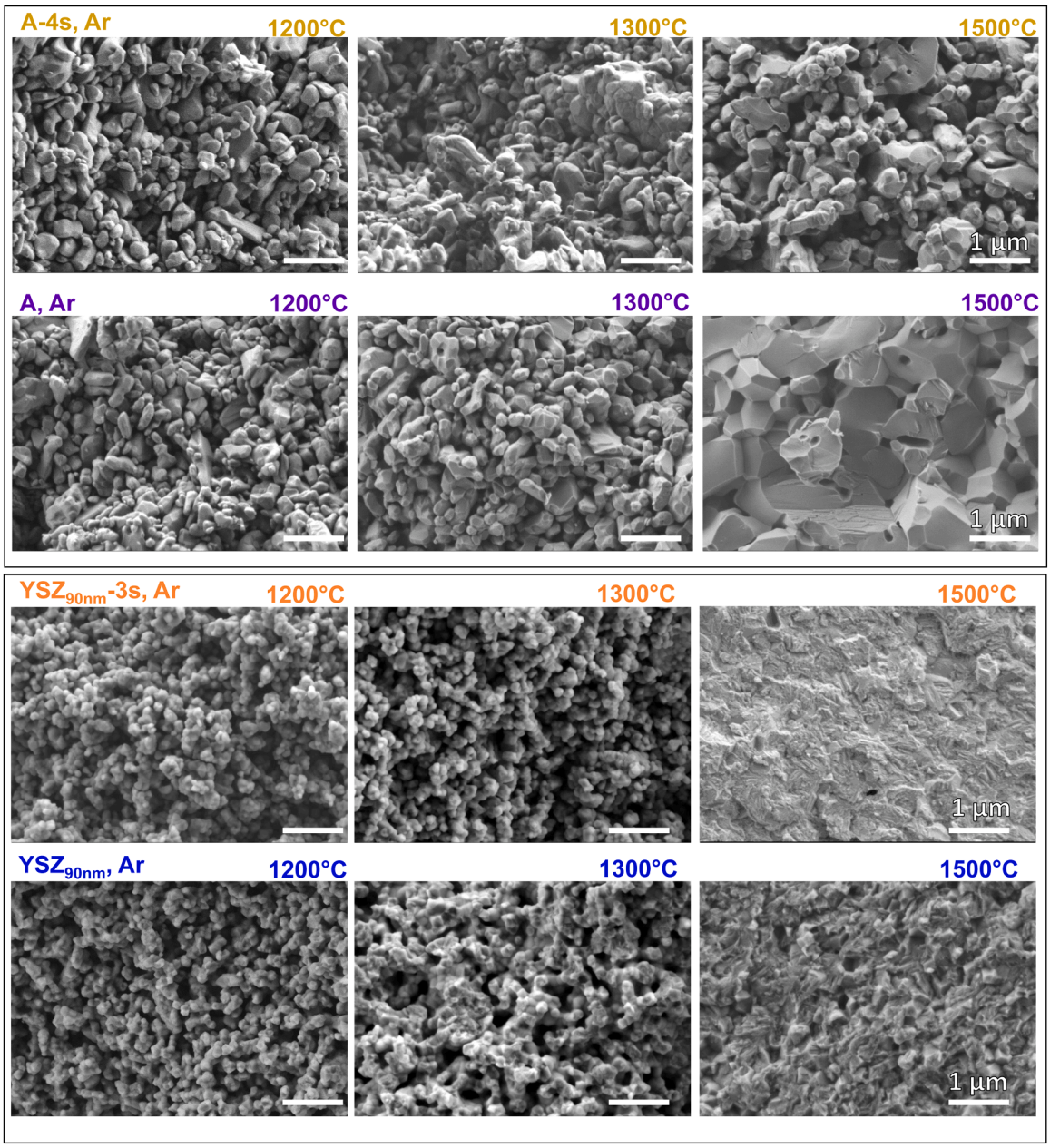

Fig. 4. SEM micrographs of the fracture surface of alumina and YSZ as a function of the final sintering temperature (Ar atmosphere). The samples were pre-sintered at 1100°C, and some were infiltrated with saccharose syrup before the sintering cycle (A-4s and $YSZ_{90\ nm}$-3s). The scale-bars are all 1 µm.

"regular" (no clear inflection at 1280°C) and carbon slows down sintering "continuously" throughout all the considered sintering temperatures (Fig. 2c and Fig. 3).

The Raman spectra show that carbon is present as a second phase. This phase evolves and orders during the heat treatments as indicated by the sharpening of the D, D', and G bands when the temperature increases. The oxide matrix has an impact on the development and ordering of the carbon phase; the Raman spectra of carbon on zirconia at 1200°C are substantially broader than those on alumina at the same temperature. Moreover, a clear graphitization event occurs on alumina at 1500°C and is evidenced by the increase in the G band intensity.

Besides the dilatometric and density data, there is strong microstructural evidence of the carbon-induced densification delay (Fig. 4). The presence of carbon not only delays the densification but also coarsening and grain growth. In fact, the carbon-doped alumina sintered at 1500°C possesses a grain size similar to that of the same composition treated at 1200 or 1300°C (Fig. 4). Furthermore, the undoped alumina at 1300°C and the carbon-doped alumina at 1500°C possess a similar density (70–75%) (Fig. 3), microstructures, grain and pore size (although we can spot a slightly coarser microstructure for A-4s sintered at 1500°C), indicating a similar influence of carbon contamination on the different mass transport pathways.

Besides sintering, carbon contamination substantially alters grain growth in the late sintering stages (Figs. 6–8). This is more evident again in the case of alumina, where carbon does not react with the oxide and remains present until the end of the thermal cycle. At carbon concentrations below the solubility limit, solute drag via Gibbsian segregation of carbon to the grain boundaries reduces the grain boundary mobility [19,21], and above the solubility limit, Zener drag becomes relevant.

4.2. *Kinetic effects of carbon and possible interpretations*

To quantitatively evaluate the impact of carbon on densification, we can use the equations for the combined sintering stage model by Hansen

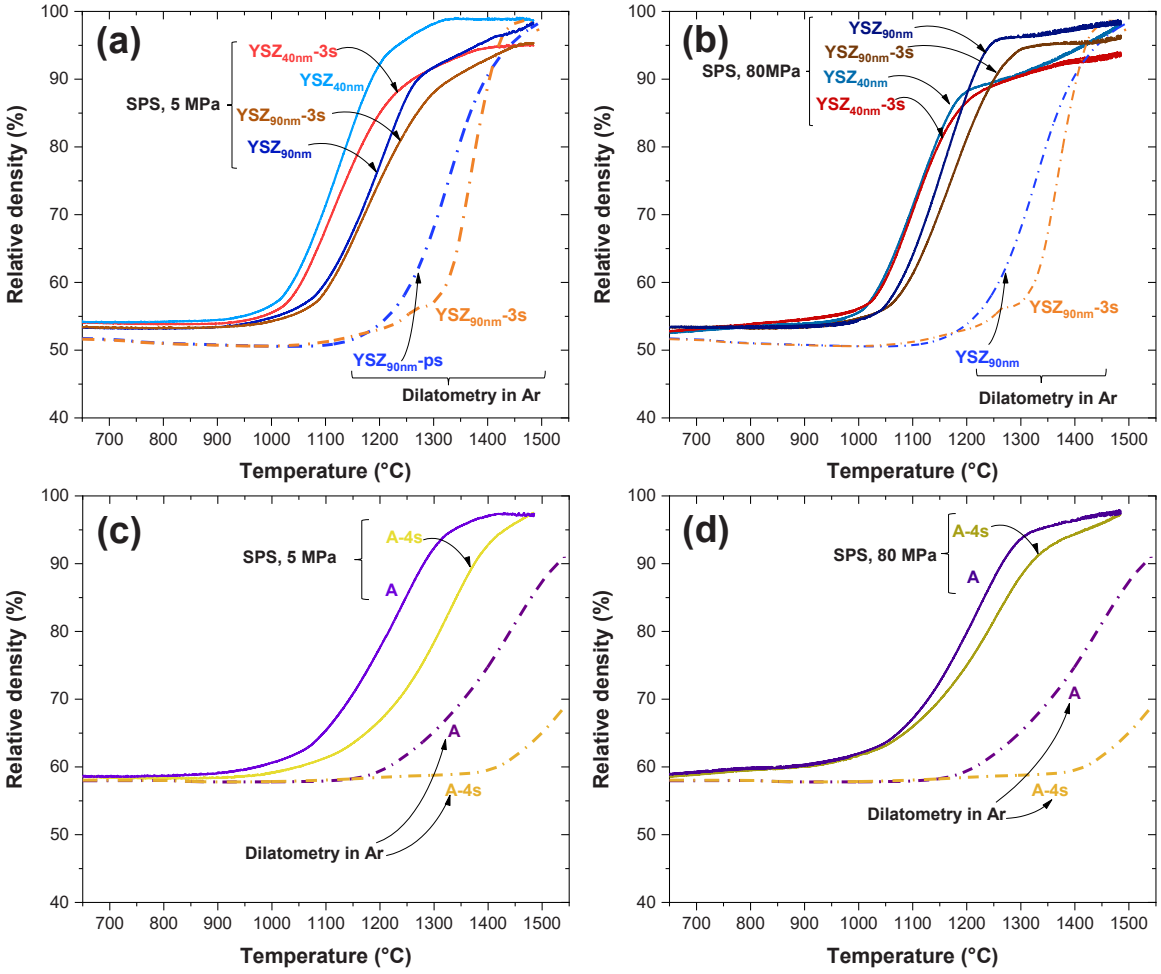

Fig. 5. Estimated densification curves of (a,b) YSZ and (c,d) alumina under (a,c) 5 and (b,d) 80 MPa in SPS. The density evolution extrapolated from the dilatometric analysis is also reported in a dashed-dot line for comparison. The samples were pre-sintered at 1100°C, and some were infiltrated with saccharose syrup before the sintering cycle (i.e., those labeled with the wt% of saccharose, s, 3 s and 4 s).

and co-workers [37], which are derived from the generalized sintering equation from the work of Wang and Raj [38]. We can re-organize the sintering equations as follows:

$$\dot{\varepsilon} = F_{(\rho,G,\gamma)} \frac{\exp(-Q/RT)}{T} \quad (1)$$

where $\dot{\varepsilon}$ is the strain rate, Q is the activation energy for the controlling mass transport mechanism, R is the ideal gas constant, T is the absolute temperature, and $F_{(\rho,G,\gamma)}$ is a function of the material microstructure, depending on density (ρ) and grain size (G). $F_{(\rho,G,\gamma)}$ also includes other constants like the pre-exponential constant for diffusion, the ideal gas constant, the stress intensity factor, surface tension, and atomic volume. Note that herein, it is assumed that the activation energy for sintering mass transport is not affected by carbon doping (i.e., we assume that the diffusion pathway remains unchanged).

It is possible to extrapolate the strain rate from the dilatometric data as well as the density evolution (assuming isotropic strain). The activation energy that can be used to model the sintering process is assumed to be about 650 kJ.mol^{-1} for YSZ (taken from a recent work on a similar powder [39,40]) and in the range 500–600 kJ.mol^{-1} for alumina [41–43]. While these activation energies might slightly vary between different powders of the same system (depending on the initial particle size or by altering the particle packing in the powder bed or green body, as well as the size and morphology of the pores) [44], we stress that the conclusions we derive are not substantially sensitive to these variations (e.g., changing Q for alumina between 500 and 600 kJ.mol^{-1} does not change our conclusions).

Under these assumptions, we can estimate $F_{(\rho,G,\gamma)}$ for the different samples and plot it against the material density (Fig. 11). Note that at a given temperature $F_{(\rho,G,\gamma)}$ is proportional to the strain rate. We can observe that:

i. If a large amount of carbon is present (≈ 5 wt%) and added from the beginning of the process, $F_{(\rho,G,\gamma)}$ is reduced by 2–4 orders of magnitude in YSZ (Fig. 11a).
ii. The reduction is much less pronounced when considering YSZ containing only ≈ 0.5 wt% carbon, introduced by the syrup-infiltration (Fig. 11b). In this case, the presence of carbon reduces the strain rate by less than 1 order of magnitude for most of the densification pathway, and eventually, in the late sintering stage, the sample infiltrated with the syrup sinters even slightly faster than the one that was not impregnated. However, we note that in that temperature/density region, carbon has already largely reacted with YSZ and has been removed from the system (see the discussion on the Raman spectra).
iii. In the case of alumina (Fig. 11c), the $F_{(\rho,G,\gamma)}$ *vs.* ρ plots are relatively regular and possess a similar dependence on density for both the carbon-containing and carbon-less materials. However, there is a reduction in the strain rate induced by the presence of carbon by about 2–2.5 orders of magnitude (the exact number depends on the choice of Q, but the order of magnitude of the densification delay is invariant).

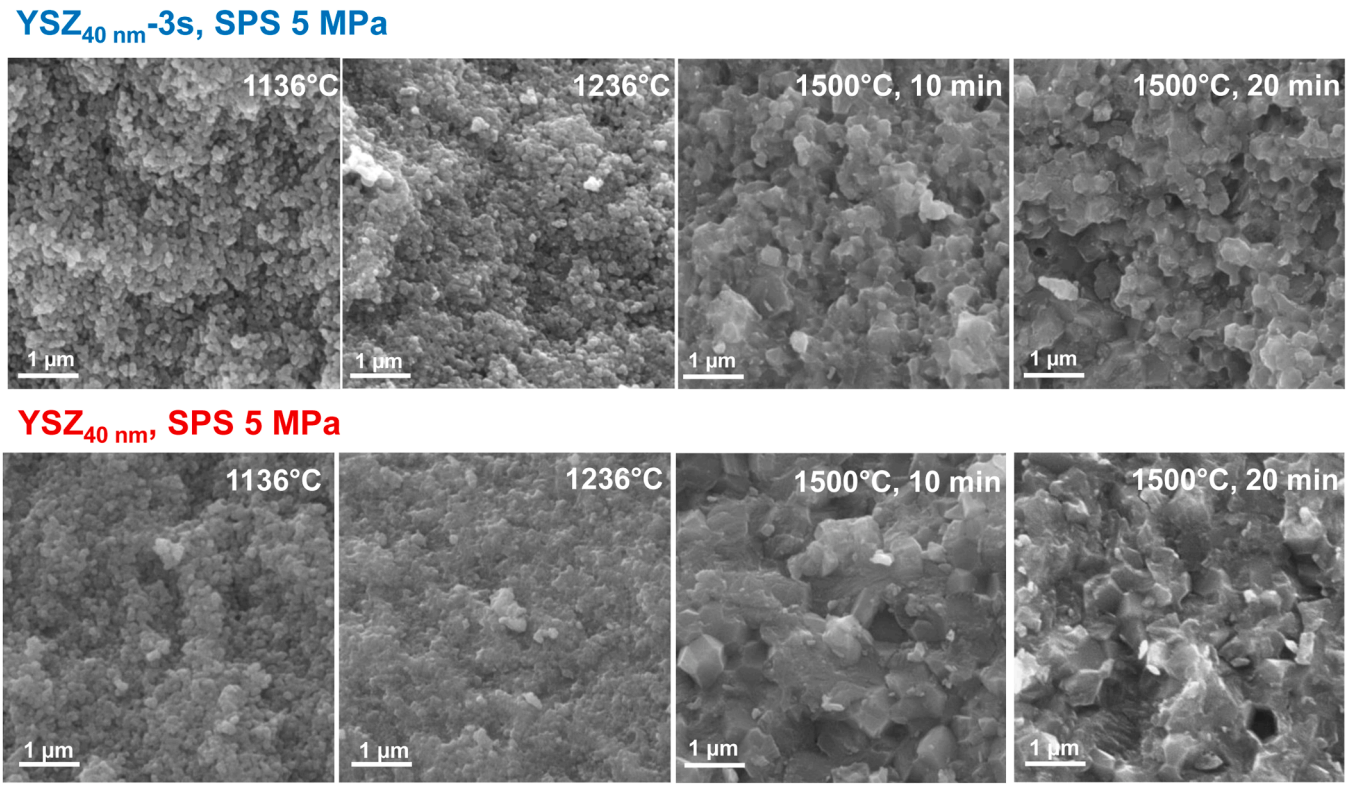

Fig. 6. SEM micrographs of the fracture surface of YSZ obtained after interrupted SPS cycles at different temperatures under 5 MPa. The samples were pre-sintered at 1100°C, and some were infiltrated with saccharose syrup before the sintering cycle ($YSZ_{40\ nm}$-3s).

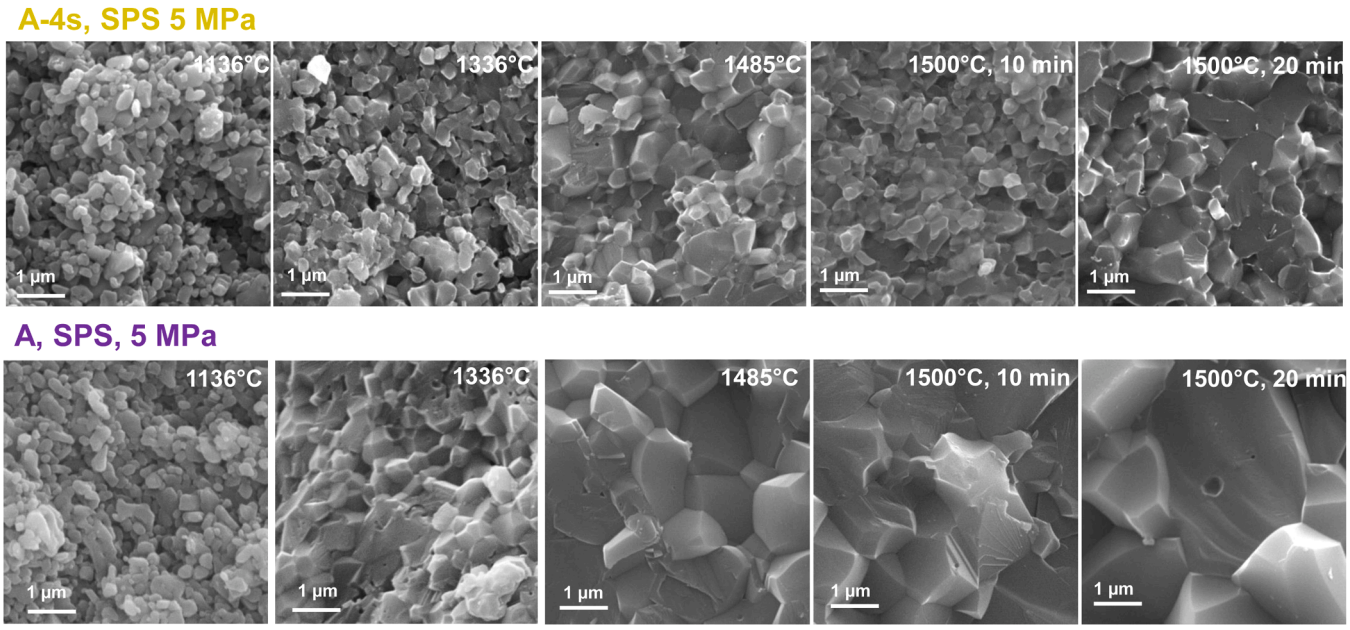

Fig. 7. SEM micrographs of the fracture surface of alumina obtained after interrupted SPS cycles at different temperatures under 5 MPa. The samples were pre-sintered at 1100°C, and some were infiltrated with saccharose syrup before the sintering cycle (A-4s).

iv. Remarkably, the sintering delay detected by dilatometry in the presence of carbon is still detectable and strong when the saccharose is added to pre-sintered materials (Fig. 2b,c and Fig. 11b, c), i.e., to materials where interparticle necking has already started to form before the addition of the carbon. Hence, a physical separation between the oxide particles induced by the carbon layer does not appear to be a reasonable explanation for the slow consolidation.

There are several possible reasons behind this carbon-induced reduction in the function *F*. Indeed, the mass flux of the *i*-th species controlling sintering is governed by:

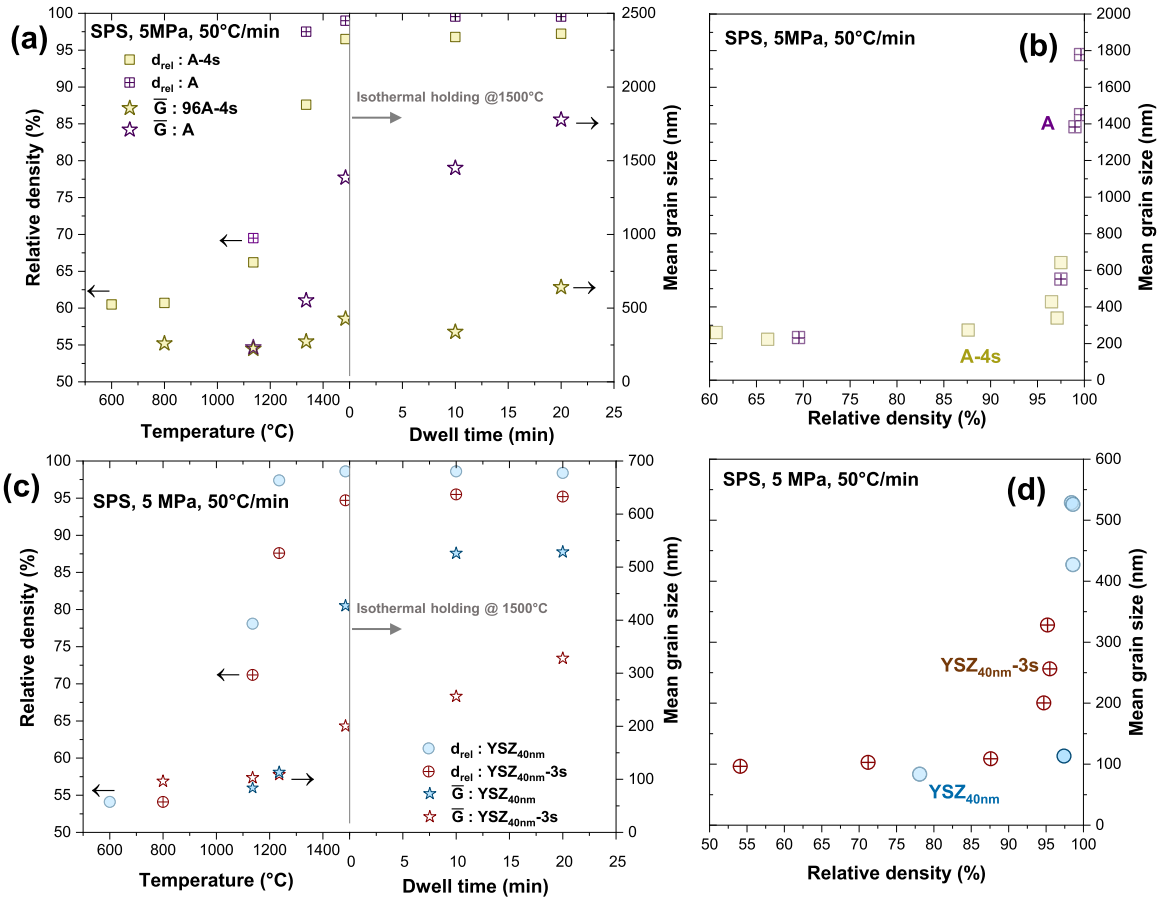

Fig. 8. (a,c) Density and grain size evolution of YSZ and alumina samples obtained by interrupting the SPS cycle (5 MPa) at different temperatures. (c,d) reports the density-grain size relation. The samples were pre-sintered at 1100°C, and some were infiltrated with saccharose syrup before the sintering cycle (those labeled as 3 s or 4 s).

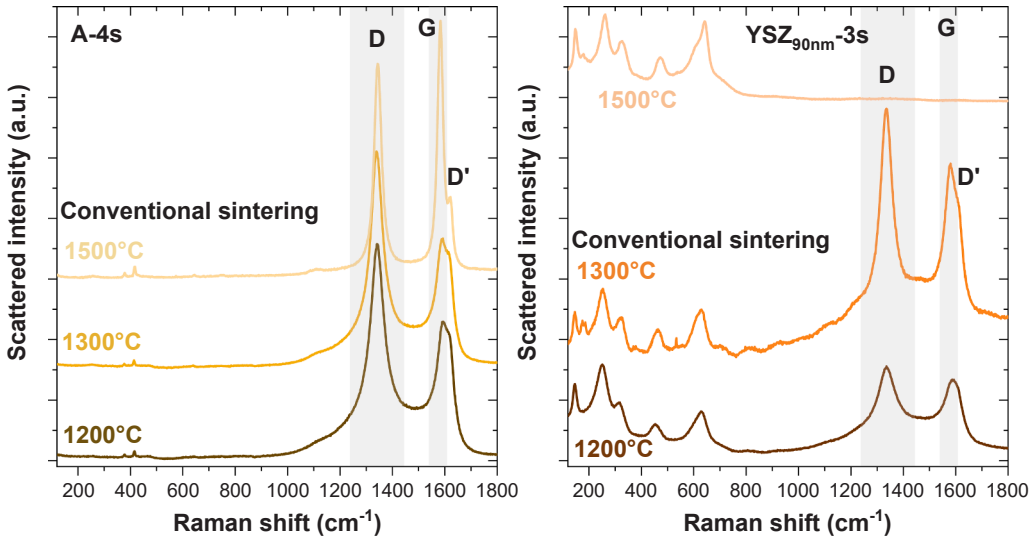

Fig. 9. Raman spectra obtained on the center (fracture surface) of conventionally sintered YSZ and alumina at different temperatures in Ar. The samples were pre-sintered at 1100°C and infiltrated with saccharose syrup before the sintering cycle.

$$\vec{J_i} = -\frac{C_i D_i}{RT} \nabla \mu_i \quad (2)$$

where C_i is the concentration of mobile defects (either vacancies or interstitials), D_i is the diffusion coefficient of the said defect and μ_i is its chemical potential. Obviously, D_i always contains a thermal activation term. The chemical potential gradient depends on three additional factors: (i) the characteristic diffusion distance (Δx), which to a first approximation can be considered half of the inter-pore distance; (ii) the pore curvature (k); and (iii) the surface energy (γ). Herein, we neglect

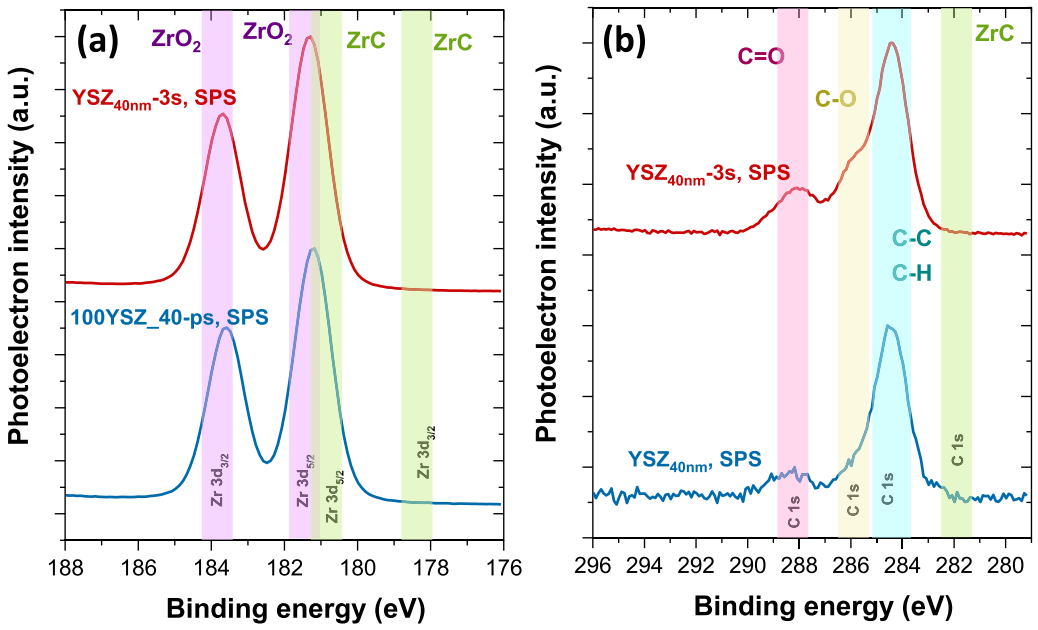

Fig. 10. (a) Zr3d and (b) C 1 s XPS spectra obtained from YSZ sintered by SPS at 5 MPa and up to 1500°C. The samples were pre-sintered at 1100°C. The blue line represents pure YSZ samples, and the red line represents samples infiltrated with saccharose syrup before the sintering cycle.

the grain boundary energy:

$$\frac{\Delta\mu_i}{\Delta x} = \frac{k\gamma\Omega_i}{\Delta x} \tag{3}$$

with Ω_i being the molar volume. The product $k\gamma$ represents the hydrostatic pressure inducing mass flow toward the porosity. Therefore:

$$J_{i,\ x} = -\frac{C_i D_i}{RT}\frac{k\gamma\Omega_i}{\Delta x} \tag{4}$$

It can be directly inferred that a change in the sintering behavior might be induced by:

(i) a change in the defect concentration or diffusivity (C_iD_i);
(ii) a change in the microstructure, e.g., Δx or k are different for a fixed level of density;
(iii) a change in γ, the surface energy.

To clarify the mechanisms, the SPS-sintered materials provide a substantial contribution. Herein, the densification curves of carbon-doped and undoped samples become similar to each other, and in some cases even overlap (Fig. 5**,8**). Even if a relatively "small" pressure (5 MPa) is applied, the density difference between carbon-containing and carbon-free samples is substantially reduced compared to the pressure-less sintering case (the density difference under 5 MPa during sintering is less than ½ that from sintering in the tube furnace). The microstructural analysis has shown that in the early/intermediate sintering stages, the grain/particle size appears not substantially affected by the presence of carbon at a fixed density level (Figs. 4 and 8), and if any difference exists, it is certainly not large enough to explain a loss in the sintering kinetics by 2 orders of magnitude in presence of carbon (Fig. 11c). In summary, the microstructure cannot easily explain the remarkable difference in the sinterability with or without carbon.

When an external pressure (p) is added, it will contribute to the driving force for mass flow, being additive with the capillarity pressure. Hence, Eq. 4 becomes:

$$J_{i,\ x} = -\frac{C_i D_i}{RT}\frac{(k\gamma + \phi p)\Omega_i}{\Delta x} \tag{5}$$

where ϕ is a density-dependent shape factor.

Let's assume now that the presence of carbon modified the defect chemistry, reducing, for instance, the defect concentration or their diffusivity (C_iD_i). If this were the case, then the addition of p to the sintering potential would accelerate the densification of both carbon-containing and carbon-free samples through a similar dynamic. In other words, if carbon substantially impacted the kinetic component of Eq. 5, then the application of the external pressure in SPS should not allow the sintering curves of the doped and undoped samples to become similar or even overlap. In summary, if carbon alters the oxide defect chemistry and/or atomic mobility, this effect should be equally present in both pressureless and pressure-assisted sintering.

Therefore, a reasonable explanation is that the addition of carbon results in Gibbsian adsorption to the surfaces, necessarily reducing the surface energy, and thus the driving force for sintering. When an external driving force is added (external pressure in SPS), the contribution of the term $k\gamma$ in Eq.5 is reduced, and the sintering behavior is less affected by carbon contamination. Ideally, when the capillarity component is negligible, the carbon effect also becomes nearly negligible, as observed in some SPS experiments under 80 MPa. Note that additional effects may still exist, but the pressure dependence of the carbon effect on densification suggests that its predominant impact is on the process thermodynamics.

Actually, the surface energy of graphite is about 0.06 J.m^{-2} [45] which is more than one order of magnitude smaller than that of a typical oxide. For example, the surface energy of sapphire on the basal plane is 1.279 ± 0.078 J.m^{-2} [46], and the GB energy is roughly half of that figure [24]. While this difference is large, it is still lower than the said reduction in $F_{(\rho,G,\gamma)}$ for alumina (i.e., the oxide system where carbon was more stable). This can be explained based on the fact that the driving force for sintering must also account for the grain boundary component (γ_{GB}) [47] to the energy excess of the polycrystal, $F_{(\rho,G,\gamma)}\ \alpha\ 2\gamma - \gamma_{GB}$. Therefore, $F_{(\rho,G,\gamma)}$ approaches zero (no sintering condition) if $\gamma = \gamma_{GB}/2$. Assuming that the grain boundary energy is about 50% of the surface energy, then one can estimate γ_{GB} for alumina to be of the order of 0.6 J.m^{-2}. Hence, an average surface energy reduction by adsorption of carbon to values of about 0.3 J.m^{-2} is enough to nullify the sintering kinetics (at a fixed grain boundary energy).

We also note that the SPS densification curves in Fig. 5 suggest that the presence of carbon does not significantly affect the sintering onset,

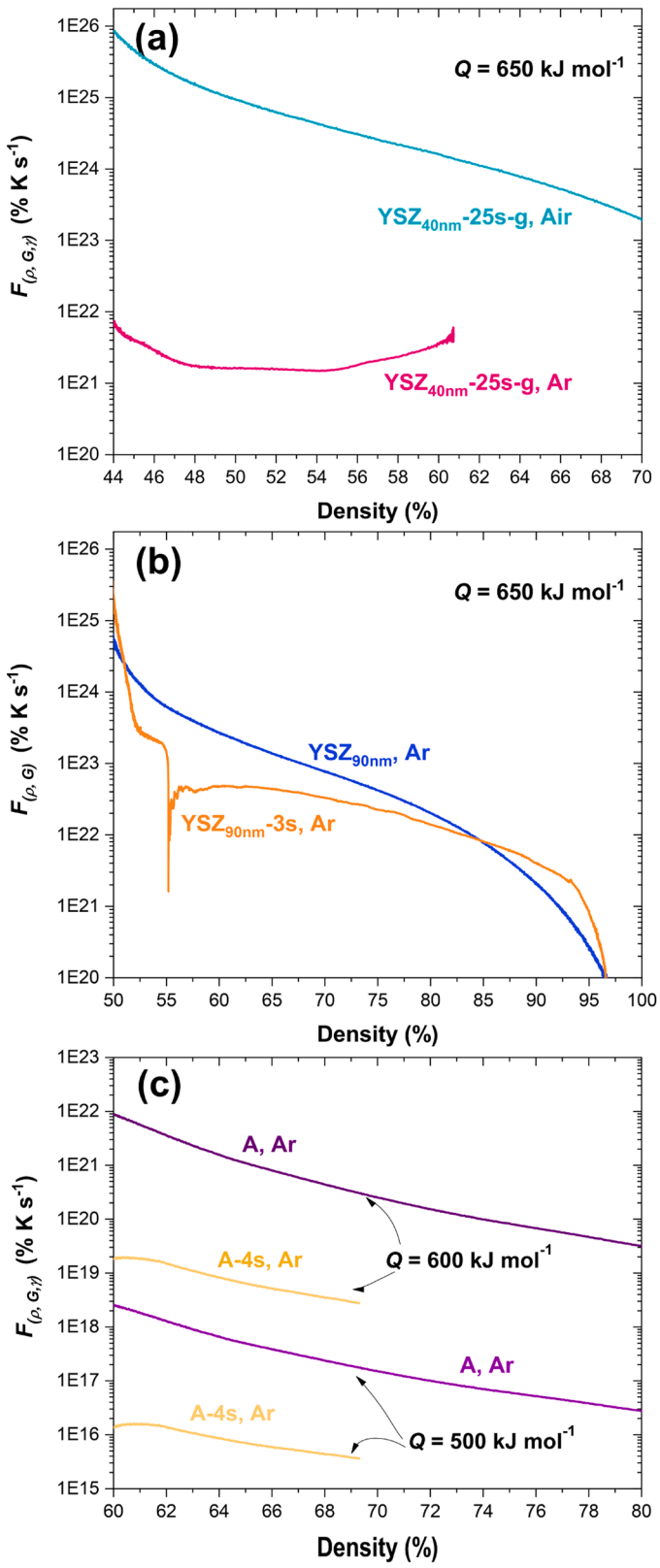

Fig. 11. $F_{(\rho,G,\gamma)}$ determined from the dilatometric data in Fig. 2 using Eq.1. (a) comparison between YSZ containing 25 wt% of saccharose fired in air and Ar; (b) comparison between $F_{(\rho,G,\gamma)}$ of pre-sintered YSZ with and without infiltration of saccharose (Ar); (c) comparison between pre-sintered alumina with and without infiltration of saccharose.

while most of the difference emerges in the intermediate sintering stages. This could be explained based on the fact that the shape factor, ϕ, decreases when the density increases (Eq.5). In other words, the external pressure effect (covering the surface energy-related driving force) could be much stronger at the sintering onset in SPS, causing the sintering curves to overlap in the early stages in SPS. This behavior cannot be noticed for pressure-less sintering, where the sintering onset is substantially shifted by the carbon incorporation, especially in Fig. 2a,c, and at high temperature, the curves get closer. This might reflect a redistribution of the carbon phase that (i) might be partially removed from the system by reacting with the oxide or oxygen impurities; (ii) might diffuse toward the grain boundary, reducing the grain boundary energy excess and therefore increasing the driving force for sintering.

A second possible interpretation of the results is based on the concept that carbon is a substantially inert phase forming a kind of rigid cage around the oxide particles, which inhibits the atomic flux towards the surface of the neck. This second interpretation is possible, although the authors consider it less plausible. In fact, graphite does not possess substantial resistance to shear and could be deformed to accommodate atoms on the surface of the necks. Moreover, the carbon layer is expected to be extremely thin: one or a few atomic layers. Considering a density for graphite of 2 g.cm^{-3}, the particle size of the powder, the maximum carbon load (Table 1), extremely limited solubility of carbon in the oxide crystal, and a homogeneous carbon thickness, one can estimate that the carbon layer should be about 0.1–0.8 nm (note that the interlayer thickness for sp^2 carbon is roughly 0.3 nm).

Moreover, we note that a change in the sintering atmosphere causes an instantaneous change in the sintering behavior (Fig. 2). This is again consistent with the hypothesis that the densification is mostly related to the presence of a surface carbon phase or segregated carbon, which can be readily removed when air is introduced in the dilatometer. On the other hand, if the effect were mostly related to a defect chemistry change due to the (aliovalent) carbon incorporation in the lattice, its removal would not be instantaneous as it would require the carbon defects to diffuse toward the surface to react with oxygen.

While the external pressure in SPS makes the sintering curves closer (with and without C doping), they do not perfectly overlap, and still, some carbon-induced delays can be spotted. These can reflect kinetic effects associated, for instance, with changes in the defect chemistry (e.g., vacancy concentration or mobility). In summary, the results indicate an enormous impact of carbon on the densification rates. Our interpretation is based mainly on thermodynamic reasoning, but additional secondary kinetic contributions (defect mobility and concentration) are also likely present.

These results are of broad relevance. Different processes can introduce carbon contamination in oxides (e.g., as a result of a debinding process) or intentional carbon doping can be used to tailor the mechanical or functional properties of an oxide. Moreover, we note that in situ sintering or coarsening experiments inside TEM might also be affected by the presence of a carbon grid and carbon adsorption.

5. Conclusions

The presence of a “small” amount of carbon (≈ 0.5 wt%) causes a substantial delay in sintering YSZ and alumina. This phenomenon is also visible in the case of carbon added to pre-sintered bodies; therefore, it cannot be attributed just to a physical separation of the oxide particles induced by the presence of a carbon phase. The sintering kinetics are reduced by a factor that can even approach 10^2. The carbon-induced sintering delay is larger for alumina than YSZ, as the latter reacts with carbon, being partially reduced and therefore removing carbon from the system.

We attribute this delay to a reduction in the driving force for sintering related to the low surface energy of the carbonaceous phases. This is confirmed by the fact that in pressure-assisted sintering experiments in SPS, the influence of carbon is reduced or completely vanishes.

However, secondary phenomena related to changes in the defect chemistry and atom mobility can also play a role.

Besides sintering, coarsening phenomena are also substantially retarded.

CRediT authorship contribution statement

Claude Estournès: Writing – review & editing, Supervision, Resources, Conceptualization. **Thomas Herisson de Beauvoir:** Writing – review & editing, Supervision. **Rachel Marder:** Writing – review & editing, Investigation. **Mattia Biesuz:** Writing – original draft, Visualization, Supervision, Resources, Methodology, Conceptualization. **Wayne D. Kaplan:** Writing – review & editing, Supervision, Resources, Conceptualization. **Rajat Chaudhary:** Investigation. **Levent Karacasulu:** Methodology, Investigation. **Etienne Martin:** Writing – original draft, Visualization, Investigation, Data curation.

Declaration of Competing Interest

The authors declare that they have no known competing financial interests or personal relationships that could have appeared to influence the work reported in this paper.

References

[1] H. Porwal, S. Grasso, M.J. Reece, Review of graphene–ceramic matrix composites, Adv. Appl. Ceram. 112 (2013) 443–454, https://doi.org/10.1179/174367613X13764308970581.

[2] H. Porwal, P. Tatarko, S. Grasso, J. Khaliq, I. Dlouhý, M.J. Reece, Graphene reinforced alumina nano-composites, Carbon N. Y 64 (2013) 359–369, https://doi.org/10.1016/j.carbon.2013.07.086.

[3] G. Fele, M. Biesuz, P. Bettotti, R. Moreno, V.M. Sglavo, Flash sintering of yttria-stabilized zirconia/graphene nano-platelets composite, Ceram. Int. 46 (2020) 23266–23270, https://doi.org/10.1016/j.ceramint.2020.06.008.

[4] X. Zhang, C. Sun, H. Ji, M. Yang, H. Zhang, W. Tian, Y. Wu, O.V. Tolochko, Y. Wang, A review of CNTs and graphene reinforced YSZ nanocomposites: preparation, mechanical and anti-irradiation properties, J. Mater. Sci. Technol. 167 (2023) 27–49, https://doi.org/10.1016/j.jmst.2023.03.068.

[5] A. Peigney, F.L. Garcia, C. Estournès, A. Weibel, C. Laurent, Toughening and hardening in double-walled carbon nanotube/nanostructured magnesia composites, Carbon N. Y 48 (2010) 1952–1960, https://doi.org/10.1016/j.carbon.2010.01.063.

[6] A. Weibel, A. Flaureau, A. Pham, G. Chevallier, J. Esvan, C. Estournès, C. Laurent, One-step synthesis of few-layered-graphene/alumina powders for strong and tough composites with high electrical conductivity, J. Eur. Ceram. Soc. 40 (2020) 5779–5789, https://doi.org/10.1016/j.jeurceramsoc.2020.06.029.

[7] K. Markandan, J.K. Chin, M.T.T. Tan, Enhancing electroconductivity of yytria-stabilised zirconia ceramic using graphene platlets, Key Eng. Mater. 690 (2016) 1–5, https://doi.org/10.4028/www.scientific.net/KEM.690.1.

[8] D. Marinha, M. Belmonte, Mixed-ionic and electronic conduction and stability of YSZ-graphene composites, J. Eur. Ceram. Soc. 39 (2019) 389–395, https://doi.org/10.1016/j.jeurceramsoc.2018.09.016.

[9] A. Gómez-Gómez, C. Ramírez, J. Llorente, A. Garcia, P. Moreno, H. Reveron, J. Chevalier, M.I. Osendi, M. Belmonte, P. Miranzo, Improved crack resistance and thermal conductivity of cubic zirconia containing graphene nanoplatelets, J. Eur. Ceram. Soc. 40 (2020) 1557–1565, https://doi.org/10.1016/j.jeurceramsoc.2019.12.016.

[10] O. Guillon, J. Gonzalez-Julian, B. Dargatz, T. Kessel, G. Schierning, J. Räthel, M. Herrmann, Field-assisted sintering technology/spark plasma sintering: mechanisms, materials, and technology developments, Adv. Eng. Mater. 16 (2014) 830–849, https://doi.org/10.1002/adem.201300409.

[11] Z.A. Munir, U. Anselmi-Tamburini, M. Ohyanagi, The effect of electric field and pressure on the synthesis and consolidation of materials: a review of the spark plasma sintering method, J. Mater. Sci. 41 (2006) 763–777, https://doi.org/10.1007/s10853-006-6555-2.

[12] K.E. Smetanina, P.V. Andreev, A.V. Nokhrin, E.A. Lantsev, V.N. Chuvildeev, Carbon contamination during spark plasma sintering of powder materials: a brief overview, J. Alloy. Compd. 973 (2024) 172823, https://doi.org/10.1016/j.jallcom.2023.172823.

[13] C. Wang, W. Ping, Q. Bai, H. Cui, R. Hensleigh, R. Wang, A.H. Brozena, Z. Xu, J. Dai, Y. Pei, C. Zheng, G. Pastel, J. Gao, X. Wang, H. Wang, J.-C. Zhao, B. Yang, X. (Rayne) Zheng, J. Luo, Y. Mo, B. Dunn, L. Hu, A general method to synthesize and sinter bulk ceramics in seconds, Science 368 (2020) 521–526, https://doi.org/10.1126/science.aaz7681.

[14] L. Karacasulu, C. Manière, C. Vakifahmetoglu, S. Marinel, M. Biesuz, Sintering under high heating rates, Annu. Rev. Mater. Res. 55 (2025) 203–230, https://doi.org/10.1146/annurev-matsci-080323-042441.

[15] H.-Z. Shen, L. Zhao, X.-R. Kong, R.-F. Guo, P. Shen, Ultrafast high-temperature sintering: principles, advantages, and applications, J. Eur. Ceram. Soc. 45 (2025) 117653, https://doi.org/10.1016/j.jeurceramsoc.2025.117653.

[16] M. Dadkhah, J.-M. Tulliani, A. Saboori, L. Iuliano, Additive manufacturing of ceramics: advances, challenges, and outlook, J. Eur. Ceram. Soc. 43 (2023) 6635–6664, https://doi.org/10.1016/j.jeurceramsoc.2023.07.033.

[17] S. Bhandari, O. Hanzel, M. Kermani, V.M. Sglavo, M. Biesuz, G. Franchin, Rapid debinding and sintering of alumina ceramics fabricated by direct ink writing, J. Eur. Ceram. Soc. 45 (2025) 117144, https://doi.org/10.1016/j.jeurceramsoc.2024.117144.

[18] S. Bhandari, C. Maniere, F. Sedona, E. De Bona, V.M. Sglavo, P. Colombo, L. Fambri, M. Biesuz, G. Franchin, Ultra-rapid debinding and sintering of additively manufactured ceramics by ultrafast high-temperature sintering, J. Eur. Ceram. Soc. (2023), https://doi.org/10.1016/j.jeurceramsoc.2023.08.040.

[19] S. Bhandari, T. Heim, E. De Bona, V.M. Sglavo, W. Rheinheimer, M. Biesuz, G. Franchin, Rapid processing of Al2O3 ceramics by fused filament fabrication and ultrafast high-temperature debinding and sintering, J. Alloy. Compd. 1017 (2025) 178812, https://doi.org/10.1016/j.jallcom.2025.178812.

[20] M. Mosadegh, M. Khakzad, Z. Sepasi, K. Nandigama, G. Kumar, M. Minary-Jolandan, Single-step thermal debinding for ceramics vat photopolymerization in less than 30 min, Ceram. Int. 51 (2025) 34846–34857, https://doi.org/10.1016/j.ceramint.2025.05.206.

[21] E.A. Marquis, N.A. Yahya, D.J. Larson, M.K. Miller, R.I. Todd, Probing the improbable: imaging C atoms in alumina, Mater. Today 13 (2010) 34–36, https://doi.org/10.1016/S1369-7021(10)70184-X.

[22] R. Marder, P. Ghosh, I. Reimanis, W.D. Kaplan, The influence of carbon on the microstructure and wear resistance of alumina, J. Am. Ceram. Soc. 104 (2021) 4214–4225, https://doi.org/10.1111/jace.17832.

[23] M. Michálek, M. Michálková, G. Blugan, J. Kuebler, Effect of carbon contamination on the sintering of alumina ceramics, J. Eur. Ceram. Soc. 38 (2018) 193–199, https://doi.org/10.1016/j.jeurceramsoc.2017.08.011.

[24] L. Cohen, P. Ghosh, A. Berner, R. Marder, W.D. Kaplan, The solubility limit of carbon in alumina at 1,600°C, Microsc. Microanal. 29 (2023) 314–325, https://doi.org/10.1017/S1431927622012491.

[25] P. Miranzo, L. Tabernero, J.S. Moya, J.R. Jurado, Effect of sintering atmosphere on the densification and electrical properties of alumina, J. Am. Ceram. Soc. 73 (1990) 2119–2121, https://doi.org/10.1111/j.1151-2916.1990.tb05282.x.

[26] Y. Hemberger, N. Wichtner, C. Berthold, K.G. Nickel, Quantification of yttria in stabilized zirconia by Raman spectroscopy, Int. J. Appl. Ceram. Technol. 13 (2016) 116–124, https://doi.org/10.1111/ijac.12434.

[27] T. Hérisson de Beauvoir, Z. Ghomari, G. Chevallier, A. Flaureau, A. Weibel, C. Elissalde, F. Mauvy, R. Chaim, C. Estournès, Flash spark plasma sintering of 3YSZ: modified sintering pathway and impact on grain boundary formation, J. Eur. Ceram. Soc. 41 (2021) 7762–7770, https://doi.org/10.1016/j.jeurceramsoc.2021.08.013.

[28] A.C. Ferrari, J. Robertson, Interpretation of Raman spectra of disordered and amorphous carbon, Phys. Rev. B 61 (2000) 14095–14107, https://doi.org/10.1103/PhysRevB.61.14095.

[29] Z. Li, L. Deng, I.A. Kinloch, R.J. Young, Raman spectroscopy of carbon materials and their composites: graphene, nanotubes and fibres, Prog. Mater. Sci. 135 (2023) 101089, https://doi.org/10.1016/j.pmatsci.2023.101089.

[30] J.-B. Wu, M.-L. Lin, X. Cong, H.-N. Liu, P.-H. Tan, Raman spectroscopy of graphene-based materials and its applications in related devices, Chem. Soc. Rev. 47 (2018) 1822–1873, https://doi.org/10.1039/C6CS00915H.

[31] L. Bokobza, J.-L. Bruneel, M. Couzi, Raman spectra of carbon-based materials (from Graphite to Carbon Black) and of some silicone composites, C. (Basel) 1 (2015) 77–94, https://doi.org/10.3390/c1010077.

[32] A. Singh, M.H. Modi, A.K. Sinha, R. Dhawan, G.S. Lodha, Study of structural and optical properties of zirconium carbide (ZrC) thin- fi lms deposited by ion beam sputtering for soft x-ray optical applications, Surf. Coat. Technol. 272 (2015) 409–414, https://doi.org/10.1016/j.surfcoat.2015.03.033.

[33] M. Biesuz, T.G. Saunders, K. Chen, M. Bortolotti, M. Salvo, S. Grasso, M.J. Reece, Interfacial reaction between ZrNbHfTa foil and graphite: formation of high-entropy carbide and the effect of heating rate on its microstructure, J. Eur. Ceram. Soc. 40 (2020) 2699–2708, https://doi.org/10.1016/j.jeurceramsoc.2019.12.011.

[34] E. Martin, U.C. Chung, M. Duttine, M.A. Dourges, G. Clermont, C. Labrugère, S. Fourcade, D. Michau, C. Estournès, T. Hérisson de Beauvoir, F. Mauvy, V. Jubera, M. Maglione, G. Goglio, C. Elissalde, Defect chemistry to trigger zirconia densification at low temperatures by Spark Plasma Sintering, Open. Ceram. 17 (2024) 100518, https://doi.org/10.1016/j.oceram.2023.100518.

[35] W.-C. Zheng, W. Fang, Y. Mei, Optical spectra and spin Hamiltonian parameters for rhombic Zr3+ in Y3Al5O12, J. Appl. Phys. 101 (2007), https://doi.org/10.1063/1.2472647.

[36] S.K. Jha, H. Charalambous, H. Wang, X.L. Phuah, C. Mead, J. Okasinski, H. Wang, T. Tsakalakos, In-situ observation of oxygen mobility and abnormal lattice expansion in ceria during flash sintering, Ceram. Int. 44 (2018) 15362–15369, https://doi.org/10.1016/j.ceramint.2018.05.186.

[37] J.D. Hansen, R.P. Rusin, M.-H. Teng, D.L. Johnson, Combined-stage sintering model, J. Am. Ceram. Soc. 75 (1992) 1129–1135, https://doi.org/10.1111/j.1151-2916.1992.tb05549.x.

[38] J. Wang, R. Raj, Estimate of the activation energies for boundary diffusion from rate-controlled sintering of pure alumina, and alumina doped with zirconia or titania, J. Am. Ceram. Soc. 73 (1990) 1172–1175, https://doi.org/10.1111/j.1151-2916.1990.tb05175.x.

[39] M. Biesuz, E. De Bona, C. Manière, Fast firing of 3 mol% yttria-stabilized zirconia: on the effect of heating rate on sintering, J. Am. Ceram. Soc. 107 (2024) 6596–6606, https://doi.org/10.1111/jace.19989.
[40] J. Dong, V. Pouchly, M. Biesuz, V. Tyrpekl, M. Vilémová, M. Kermani, M. Reece, C. Hu, S. Grasso, Thermally-insulated ultra-fast high temperature sintering (UHS) of zirconia: a master sintering curve analysis, Scr. Mater. 203 (2021) 114076, https://doi.org/10.1016/j.scriptamat.2021.114076.
[41] A. Talimian, V. Pouchly, H.F. El-Maghraby, K. Maca, D. Galusek, Impact of high energy ball milling on densification behaviour of magnesium aluminate spinel evaluated by master sintering curve and constant rate of heating approach, Ceram. Int. 45 (2019) 23467–23474, https://doi.org/10.1016/j.ceramint.2019.08.051.
[42] J. Tatami, Y. Suzuki, T. Wakihara, T. Meguro, K. Komeya, Control of shrinkage during sintering of alumina ceramics based on master sintering curve theory, Key Eng. Mater. 317–318 (2006) 11–14, https://doi.org/10.4028/www.scientific.net/KEM.317-318.11.
[43] B. Baruah, R. Anand, S.K. Behera, Master sintering curve and activation energy of sintering of ZrO2-doped Al2O3, Ceram. Int. 47 (2021) 7253–7257, https://doi.org/10.1016/j.ceramint.2020.11.001.
[44] T. Frueh, I.O. Ozer, S.F. Poterala, H. Lee, E.R. Kupp, C. Compson, J. Atria, G. L. Messing, A critique of master sintering curve analysis, J. Eur. Ceram. Soc. 38 (2018) 1030–1037, https://doi.org/10.1016/j.jeurceramsoc.2017.12.025.
[45] J. Lee, B. Lee, A simple method to determine the surface energy of graphite, Carbon Lett. 21 (2017) 107–110, https://doi.org/10.5714/CL.2017.21.107.
[46] G. Levi, W.D. Kaplan, Aluminium-alumina interface morphology and thermodynamics from dewetting experiments, Acta Mater. 51 (2003) 2793–2802, https://doi.org/10.1016/S1359-6454(03)00084-3.
[47] D. Gouvêa, Thermodynamic of solid-state sintering: contributions of grain boundary energy, J. Eur. Ceram. Soc. 44 (2024) 116677, https://doi.org/10.1016/j.jeurceramsoc.2024.116677.